PCCP

ROYAL SOCIETY OF CHEMISTRY

PAPER

View Article Online
View Journal | View Issue

Cite this: *Phys. Chem. Chem. Phys.*, 2025, **27**, 25116

Specific and non-specific interactions of fibronectin with zwitterionic peptoid brushes studied by molecular dynamics simulation

David L. Cheung, *[a] Phillip B. Messersmith [bcd] and King Hang Aaron Lau *[e]

Received 18th June 2025,
Accepted 27th October 2025

DOI: 10.1039/d5cp02324f

rsc.li/pccp

Zwitterionic polymer brushes represent a prominent class of surfaces to prevent non-specific protein interactions. However, residual protein binding and cell attachment can still be observed. Peptide-mimetic "peptoids" constitute a versatile sequence-specific platform for developing specific protein binding motifs as well as antifouling brushes. Nonetheless, molecular level insight into their protein interactions is generally lacking. Using atomistic molecular dynamics (MD) simulation, we analyse the interactions of fibronectin type-III (FnIII) 9- and 10-domains with a zwitterionic peptoid brush and compare it with polysarcosine, the well-known and uncharged elementary peptoid and potential PEG replacement. Experimental protein adsorption trends are used to determine the peptoid chain densities simulated. For each combination of peptoid and chain density, 9 independent simulations with different starting protein orientations are performed. The simulation results are consistent with experimental measurements over different chain densities, and they identified $FnIII_{9\text{-}10}$ regions and specific amino acids with typical involvement in interactions with polysarcosine and the zwitterionic variant. Moreover, stronger interactions are seen for the zwitterionic peptoid design, and the protein's integrin binding motifs face away from the surface, nearly opposite in direction to the sequence segments interacting with the peptoids. These observations give new insight into protein–peptoid interactions and suggest the possibility of designing peptoid sequences for presenting cell-binding protein motifs and mediating cell attachment.

1. Introduction

Surfaces that can control the specific and non-specific binding of proteins are important in many applications.[1,2] Non-specific adsorption onto medical implants can lead to unfavourable immune and inflammatory responses[3] and biofilm formation.[3] Specific interactions can control cell growth for the creation of living biomaterials.[4,5] A wide-range of surfaces have been investigated to suppress non-specific protein adsorption,[6,7] particularly surface grafted zwitterionic polymer brushes.[8] However, due to the interplay between factors such as surface hydration, electrostatic potential, and steric effects, understanding the origins of non-specific adsorption behaviour, and correspondingly the antifouling effect of zwitterionic brushes, are challenging.[9]

Peptoids (*N*-substituted glycines) are peptide-mimetic molecules[10,11] with side chain attachment shifted from the alpha carbon to the amide nitrogen, which renders the peptoid backbone achiral and enables both *cis*- and *trans* conformations. Moreover, by substituting the amide hydrogen atom with the sidechain, the backbone presents solely hydrogen bond (H-bond) acceptors, precluding intra-backbone H-bonding and favouring backbone interactions with water or other H-bond donors in the environment. In this regard, one of us first reported that polysarcosine, the simplest polypeptoid with single methylenes as sidechains and the analogue of polyalanine, may form highly hydrated and excellent antifouling polymer brushes, which are being pursued as a polyethylene glycol (PEG) replacement.[12–14] Additionally, peptoids can be synthesised with precise lengths and sequences using solid-phase techniques to investigate their use as therapeutics and as models of polymer design, including zwitterionic brushes.[15,16]

Understanding the interaction between proteins and surfaces requires knowledge of interactions and processes on the molecular level. However, experimental methods have mostly provided surface averaged results. Surface optical[17] and quartz crystal microbalance[18] techniques have been most commonly used to determine the total amount of protein binding. Other

[a] *School of Biological and Chemical Sciences, University of Galway, Galway, Ireland. E-mail: david.cheung@universityofgalway.ie*
[b] *Department of Bioengineering, University of California, Berkeley, USA*
[c] *Department of Materials Science and Engineering, University of California, Berkeley, CA 94720, USA*
[d] *Materials Sciences Division, Lawrence Berkeley National Laboratory, Berkeley, CA 94720, USA*
[e] *Department of Pure and Applied Chemistry, University of Strathclyde, Glasgow, UK. E-mail: aaron.lau@strathclyde.ac.uk*

surface specific techniques such as neutron reflectivity,[19,20] sum frequency generation spectroscopy[21] and surface force apparatus[22] can give insight into the structure of surface layers and hydration. While atomic force microscopy can characterise single protein–surface interactions, they require expertise in liquid AFM and tip biointerface preparation.[23,24]

To complement experiments, many molecular dynamics (MD) studies over the past two decades have investigated protein adsorption/binding onto surfaces.[25] These studies have given significant insight into the molecular factors that control protein adsorption, such as the role of surface bound water, surface structure,[26,27] and surface chemistry.[28] Earlier studies have often focused on simple surfaces, such as metals[29] or silica,[30] and self-assembled monolayers,[31] although increasingly more complex surfaces have been studied, such as polymers[32,33] (crystalline or amorphous) and brushes.[34] These have identified features such as surface hydration and mobility that are correlated with protein resistance,[35,36] and we have found that zwitterionic peptoids can be more hydrated and provide a higher electrostatic potential than an uncharged control.[36] Nonetheless, explicit simulation with proteins is necessary to more fully understand these factors, and there has in fact been no study yet of explicit protein interactions with peptoids.

In this paper, using MD simulations, we investigated the interaction of fibronectin (Fn) onto a sequence-specific "PSKE" zwitterionic peptoid brush based on the polysarcosine (PS) backbone. We focus on the ninth and tenth Fn type-III domains ($FnIII_{9\text{-}10}$), which contain the biologically important synergy (PHRSN) and cell-binding (RGD) motifs relevant to cell adhesion and inflammatory response.[37] While high levels of non-specific adsorption on implanted medical devices may lead to adverse effects such as fibrosis,[38] suitable Fn binding may drive the formation of Fn fibrils for the control of cell differentiation[39] and the binding of growth factors.[40] Fn surface binding may also mediate implant-associated infections because the protein is a target for a number of bacteria.[41] We also experimentally performed general protein adsorption measurements to characterize the amount of non-specific protein adsorption as a function of the grafted chain density, to inform grafting parameters for the simulations and to compare with simulation results. Multiple simulations with different starting protein orientations were performed to verify the specificity of the interactions. The results were analysed according to various protein and brush features, including the protein–peptoid interaction energy, protein orientation, residue proximity to the brush, hydrogen bonding, and the specificity of interactions according to peptoid sequence.

2. Methodology

2.1. Computational modelling

All PS and PSKE brushes consisted of 20-mer chains (Fig. 1(a)). To construct the zwitterionic PSKE, two pairs of adjacent cationic Nk (analogue of K – lysine) and anionic Ne residues (analogue of E – glutamic acid) were inserted along a PS backbone spaced apart by six uncharged sarcosine residues.

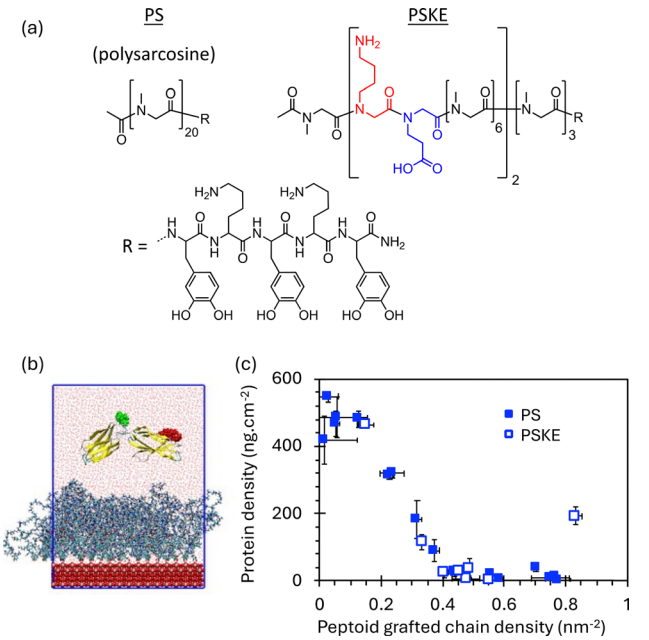

Fig. 1 (a) Chemical structures of the PS and PSKE peptoids simulated. (b) Example of initial simulation structure. PHRSN (synergy) and RGD (cell recognition) motifs highlighted as red and green spheres respectively. (c) Protein adsorption on PSKE peptoid brushes grafted over a range of surface chain densities. Comparison data for the PS control is sourced from ref. 12.

The naming of peptoid residues follow our recent proposal.[42,43] This design is analogous to "PMKE" (Fig. S1a), another anti-fouling zwitterionic peptoid we previously studied based on uncharged methoxyethyl (M) sidechains (Fig. S1a).[15,36] PSKE is considered to be of particular current interest because of its relevance to PS and its potential use as a PEG replacement.[12–14]

Based on previous work,[36] the PS and PSKE brushes were initially placed as a regular array of fully extended chains on TiO_2 rutile (110), chosen as a model biomedical implant surface. This slab was held rigid during the simulations, and had a thickness of 16 Å in the *z*-direction, 16 and 34 unit cells in the *x* and *y* directions, respectively, giving a surface area of 104.9 Å by 101.2 Å. In experiments, the peptoid was attached *via* a C-terminal pentameric motif characterized by three dihydroxyphenyl (DOPA) interspaced by two lysine residues (Fig. 1(a)). In MD simulations, the *z*-coordinate of the H_ζ atoms of the terminal DOPA residues were constrained to 1.78 Å above the highest oxygen atom in the rutile surface (corresponding to the minimum in the LJ potential between these atoms). As the constraint was only applied to the *z*-coordinate, the peptoid chains retained mobility in the plane of the surface. Note that the DOPA anchoring pentamer represents a *ca.* 15 Å thick spacer layer between the 16 Å TiO_2 slab and the peptoid chain. Thus, together with the 16 Å rutile slab, the height scale of all relevant figures in this study start at 30 Å to highlight the behaviour of the peptoid brush and the protein.

Two grafting densities, one below and the other above the expected critical grafting density, were chosen (see Section 2.2 below for densities used). Prior to the insertion of the protein,

the surfaces were solvated and chloride counter-ions added to neutralise the lysines of the anchor groups. Each surface was then energy minimized and a 100 ns MD simulation was performed to generate an initial structure for the brush. The average water densities far from the brush were verified to be physically realistic ($\sim$998 kg m^{-3} at 20 °C) (Table S1). After this equilibration, a single protein consisting of the $FnIII_{9\text{-}10}$ domains was added in the bulk liquid (Fig. 1(b)). The initial structure of the protein was taken from the protein database (1FNF[44]), with the $FnIII_9$ and $FnIII_{10}$ domains corresponding to residues 1–89 and 90–184 respectively. The $FnIII_{9\text{-}10}$ protein was placed with its centre-of-mass $\sim$8 nm from the rutile surface; this made the lowest atom–atom separation between the protein and the brush at least 2 nm. The ionization states of the protein termini and ionizable residues were set as appropriate for neutral pH (His uncharged, all other acidic and basic groups charged), and the number of counter-ions was adjusted to maintain overall charge neutrality.

The charmm27 force field,[45] extended to consider peptoids[46] and non-natural amino acids,[47] was used for the protein and brush along with the charmm-TIP3P[48] water model. The rutile surface was modelled using the potential of Predota *et al.*[49] As the rutile slab was held fixed, the interactions within the slab were neglected. The system was periodic in the x and y directions (in the plane of the surface). To contain the system within the z-direction walls, interacting through an integrated 9-3 LJ potential were used. Interactions were evaluated with a cut off of 12 Å, with corrections to the energy and pressure applied. Electrostatic interactions were evaluated using a particle-mesh Ewald sum[50] with a real space cut off of 12 Å and a reciprocal space grid of 48 × 48 × 280.

All simulations were performed using the Gromacs molecular dynamics package (version 2018.4).[51–53] The system was energy minimised using the steepest descents algorithm, followed by short (10 ps) NVT simulations. Simulations were performed at 298 K, with temperature controlled using the velocity rescaling algorithm[54] with a relaxation time of 0.1 ps. For each system, simulations of 200 ns were performed (with a timestep of 2 fs), with coordinates saved every 10 ps, giving a total simulation time of 7.2 μs across all systems. Bonds involving hydrogen atoms were constrained using the LINCS[55] algorithm and the geometry of water molecules was held rigid using the SETTLE[56] algorithm.

To sample protein orientations, for each of the four combinations of two peptoids and two brush densities, 9 separate simulations were performed (Table 1) to cover the different initial protein orientations possible with three starting lateral orientations of $FnIII_{9\text{-}10}$ (along x, along y, and at 45 degrees to the x-axis) and three starting rotational orientations of the synergy (PHRSN) and cell recognition (RGD) motifs (pointing away from surface, towards surface, and parallel to surface). Thus, 36 simulations were performed overall. All simulations started with the $FnIII_{9\text{-}10}$ long axis in the x–y plane; those starting with the protein termini oriented towards the surface were not considered since the full fibronectin protein is elongated in shape and configurations with the protein's long axis parallel to the surface are expected to be favoured in physiological conditions, unless there are specific interactions with terminal residue segments.[27] Since the equilibrated brush has no intrinsic alignment in the x–y plane, the three simulations with different lateral protein starting orientations for each peptoid–density combination may be considered replicates.

Table 1 Definition of starting proteins orientations for each simulation. See Fig. 1(b) for an illustration of initial positions of cell-binding and synergy motifs

Run	PHRSN/RGD orientation	Long axis orientation
1	Away from surface	Along x
2	Toward from surface	Along x
3	Parallel to surface	Along x
4	Away from surface	Along y
5	Toward from surface	Along y
6	Parallel to surface	Along y
7	Away from surface	45 degrees to x
8	Toward from surface	45 degrees to x
9	Parallel to surface	45 degrees to x

Analysis of the simulations was performed using standard gromacs utilities and in-house python scripts using the MDAnalysis library.[57] Hydrogen bonds were identified using a donor–acceptor cutoff of 3 Å and donor-hydrogen-acceptor angle greater than 150°. Simulation snapshots were generated using VMD[58] (visual molecular dynamics).

To estimate the adsorption free energy (ΔG_{ads}) molecular mechanics Poission–Boltzmann surface area (MM-PBSA) calculations[59] were used. ΔG_{ads} was calculated according to:

$$\Delta G_{ads} = G_{protein\text{–}surf} - G_{protein} - G_{surf} \quad (1)$$

where $G_{protein\text{–}surf}$ is the free energy of the protein–surface system and $G_{protein}$ and G_{surf} were the free energies of the protein and surface on their own. The calculations were performed using the single trajectory approach, where the free energies were calculated from a single simulation of the system. The free energy for each system was given by the sum of the molecular mechanics (E_{MM}) and solvation (G_{solv}) energies:

$$G = E_{MM} + G_{solv} = E_{MM} + G_{PB} + G_{SA} \quad (2)$$

where the solvation energy consists of polar solvation (G_{PB}) and non-polar solvation (G_{SA}) contributions. The conformation entropy is neglected due to the inaccuracy associated with its calculation and the limited influence this has on the calculated values.[60] The molecular mechanics energy was given by:

$$E_{MM} = E_{int} + E_{vdw} + E_{elec} \quad (3)$$

where the terms are the internal (bonded), VDW, and electrostatic energies. Note that for the single trajectory method the internal energy of the protein–surface complex is the same as the internal energies of the protein and surface added together, so this does not contribute to the value of the adsorption free energy. The non-polar solvation energy was calculated according to:[61]

$$G_{SA} = \gamma SASA + b \quad (4)$$

where SASA is the solvent accessible surface area, γ = 0.005 kcal mol^{-1} Å^{-2} is the surface tension, and b = 0 (appropriate for the inp = 1 option in MMPBSA.py). A probe radius of

1.4 Å was used in the calculation of SASA. The polar solvation energy was calculated using a Poisson–Boltzmann solver, with internal and external dielectric constants of 1 and 80. The former was chosen to be a low value to match the non-polar environment within the atoms while the latter matched the value of water. The MM-PBSA calculations were performed using the MMPBSA.py script,[62] part of the Amber package (version 18).

2.2. Selection of peptoid grafting density

A qualitative comparison with experimental measurements of non-specific protein adsorption was sought to indicate the grafted chain density values below and above the critical density to be used in MD simulations. A quantitative comparison was not warranted because the critical density depends on the size of the protein and its propensity to adsorb, but the full fibronectin protein (~250 kDa) is much larger than the $FnIII_{9\text{-}10}$ domains simulated (*ca.* 26 kDa) and cannot be accommodated in MD. Recombinant $FnIII_{9\text{-}10}$ also could not be obtained at high enough amounts for experiments. Therefore, fibrinogen was used as a model protein due to its size (340 kDa) and elongated shape approximating fibronectin, and it is readily available at physiologically relevant amounts (3 mg mL^{-1} in pH 7.4 hepes buffer used for measurements; see SI and ref. 12 and 15 for materials and experimental details).

Fig. 1(c) shows that adsorption decreased to its minimal at ~0.55 chain nm^{-2} for the 20-mer PSKE brush. Data for the PS control is replotted from ref. 12 for comparison. Both peptoids are seen to exhibit a very similar adsorption trend up to 0.8 chain nm^{-2}. In fact, in this range of chain densities, further comparison with the aforementioned PMKE and its uncharged control[15] indicates a common ~0.55 chain nm^{-2} critical density against fibrinogen adsorption for all brushes (Fig. S1). This suggests the behaviour may be characteristic of the poly(*N*-substituted glycine) peptoid backbone. At the same time, smaller proteins often require lower chain densities to reduce adsorption, *e.g.*, 0.3 chain nm^{-2} for serum albumin reported for PMKE.[15]

Therefore, for the present MD simulations, 12 and 60 chains on the TiO_2 slab (translating to 0.11 and 0.56 chain nm^{-2}) were chosen as the grafting densities expected to be below and above the critical density, respectively. Interestingly, larger uncertainties for the zwitterionic PSKE and PMKE than for the uncharged controls were also noticeable for adsorption around the 0.55 nm^{-2} critical density (Fig. S1(b) and (c)).[15] Moreover, new data for PSKE and PMKE >0.8 chain nm^{-2} in the same figure show that adsorption on these peptoids increased back to relatively large values (~200 ng cm^{-2}), similar to the range at lower chain densities <0.3 cm^{-2}. This behaviour is further discussed in the results section 3.3.

3. Results and discussion

3.1. Trajectories and energetics of fibronectin–brush interaction

Fig. 2 shows the evolution of the $FnIII_{9\text{-}10}$ centre-of-mass positions (z) over all the 36 trajectories simulated for 200 ns. The averaged peptoid residue densities are also shown in Fig. 2 to indicate the relative positions of the protein. The corresponding averaged water densities are shown in Fig. S2.

At the lower grafting density of 0.11 nm^{-2} (*i.e.*, Nchain = 12), below the critical density (see Methodology section 2.2), the polymer density was expected to be insufficient to resist non-specific protein adsorption. In simulations, the protein was seen to drop quickly towards the underlying titania for both the zwitterionic PSKE and the uncharged PS control. Specifically, as the simulations progressed, the centres-of-mass of $FnIII_{9\text{-}10}$ (z) came to rest between the top (~60 Å) and the base of the peptoid brushes (~30 Å), indicating penetration into the peptoid layer. In fact, the calculated interaction energy noticeably trended towards more negative values, from *ca.* −5 to −75 kcal mol^{-1}, as z decreased from *ca.* 60 Å to 40 Å (Fig. 3), indicating increasing interactions as the protein penetrated into the peptoid layer, consistent with non-specific adsorption. (See also Fig. S4 for the data plotted by simulation run number and Table S2 for the MM and solvation contributions to the adsorption free energies.) No particular trends were discerned in terms of starting protein orientation, suggesting the simulations were long enough to avoid being biased by the initial conformation.

A similar behaviour was observed for PSKE. Furthermore, at similar height positions, the interaction energies for PSKE Nchain = 12 were more negative than for the interaction of PS Nchain = 12, indicating more favourable interactions with the zwitterionic peptoid. Consistent with this observation, the simulation trajectories also showed that the protein penetration process generally took less time for PSKE than for PS (compare Fig. 2(a) and (c)).

At the higher grafting density of 0.56 nm^{-2} (*i.e.*, Nchain = 60), which is expected to be above the critical density, the simulation trajectories showed that the protein positions also

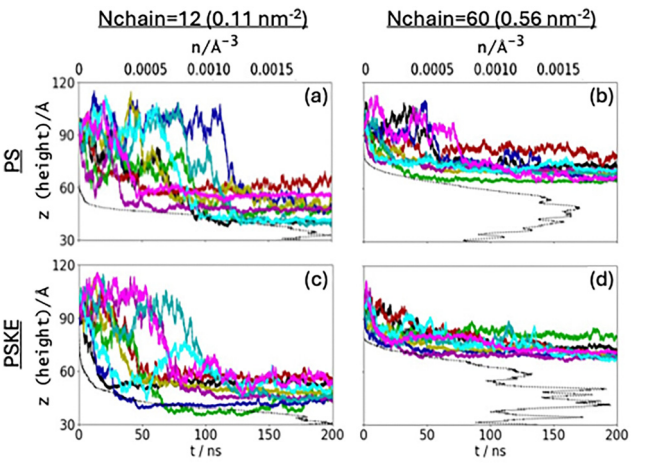

Fig. 2 Time trajectories (bottom x-axes) of protein centre-of-mass positions (z_{com}) for $FnIII_{9\text{-}10}$ on PS Nchain = 12 (a), PS Nchain = 60 (b), PSKE Nchain = 12 (c), and PSKE Nchain = 60 (d). Black, red, green, blue, yellow, purple, turquoise, cyan, and magenta denote simulation runs 1–9, respectively. Brush density distributions with height are shown in dotted black lines (top x-axes). Note that the height axes start at 30 Å, indicating the approximate starting position of the peptoid brush portion, below which are the DOPA-containing surface anchor and the TiO_2 slab.

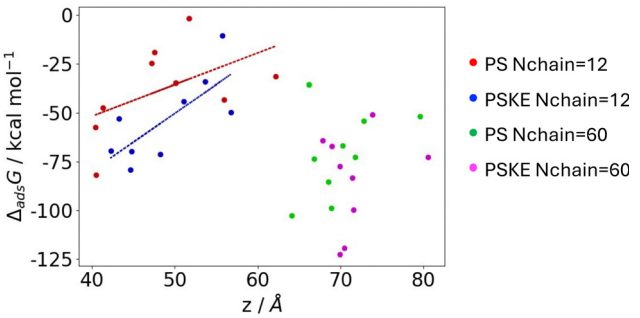

Fig. 3 Correlation between average (over the last 50 ns of the simulation) protein–surface interaction energy ($\Delta_{ads}G$) and protein centre-of-mass position (z). The red and blue lines represent linear regression fits to, respectively, the PS and PSKE Nchain = 12 data. No correlation of $\Delta_{ads}G$ with z was apparent with the Nchain = 60 data and no fits were attempted.

trended downwards (Fig. 2(b) and (d)). However, unlike at Nchain = 12, there was less variation in the final protein height position and $FnIII_{9\text{-}10}$ consistently remained above the peptoid layers. Furthermore, there was no correlation in the average adsorption free energy with the average protein centre-of-mass for either the PSKE or PS brushes—the highest and lowest interaction energies (*ca.* −10 to −120 kcal mol^{-1}) were all found around protein positions between *ca.* 65 Å and 70 Å (Fig. S3 and Fig. 3, respectively). In fact, for PS, these minimum and maximum energies were found at the two lowest positions sampled. Therefore, while energies calculated for some Nchain = 60 runs were even lower than those for Nchain = 12, they may simply reflect the higher density of peptoid chains available for interactions. Hence, the consistent interaction between $FnIII_{9\text{-}10}$ and the peptoid brush top surface centred around ∼70 Å (Fig. 2(b), (d) and 3) might represent a phenomenon such as reversible adsorption.

Nonetheless, as for Nchain = 12, the movement of the protein towards the brush took a shorter time for PSKE *vs.* PS (Fig. 2(b), (d)). The average interaction energies for PSKE Nchain = 60, like for the Nchain = 12 condition, were also observed to be overall lower than for the PS simulations (Fig. S4c and d). Therefore, the data at both chain densities suggest that PSKE may have distinct interactions from PS. The fact that these appear to be stronger was unexpected, given the literature on zwitterionic antifouling brushes.

It should be noted that while MM-PBSA calculations are commonly used in estimating binding free energies, they neglect factors such as interfacial water that can play a key role in the binding of proteins to surfaces. Although more accurate determinations of binding free energies were not carried out, the role of interfacial water was examined through bridging water molecules that simultaneously H-bond with a protein and a peptoid residue, and this was also compared with direct H-bonds between the protein and the brush (see section 3.3).

3.2. Differences in FnIII domain interactions

Comparison of the individual centres-of-mass for the $FnIII_9$ and $FnIII_{10}$ domains (Fig. S4) suggests that peptoid–protein interactions may be classified as 9-down, 10-down, or even. As defined by whether the average domain positions differed by more than the sum of their standard deviations. The number of these occurrences are summarized in Table 2, which shows that both modes for PSKE were roughly equally likely, but 10-down for PS was more common. This could be due to a relatively closer match between the lower polarity of the uncharged PS and the less hydrophilic nature of $FnIII_{10}$ (average hydrophobicity values[63] of −0.454 for $FnIII_9$ *vs.* −0.115 for $FnIII_{10}$).

To better understand the 9-down and 10-down configurations and whether specific protein sequences may be associated with peptoid interactions, simulation snapshots (Fig. 4) and the differences between the centres-of-mass of $FnIII_{9\text{-}10}$ and the individual residues (Fig. 5 and Fig. S4, S5) were further analysed. For the 9-down configuration (Fig. 4(a)), the snapshots suggest that $FnIII_9$ interactions were also associated with some degrees of $FnIII_{10}$ interactions (*i.e.*, the difference in average height of $FnIII_9$ and $FnIII_{10}$ were small, and 9-down was in fact similar to the even or a "flat" configuration). This larger protein contact interface may have contributed to the aforementioned larger interaction energies calculated for protein interactions on PSKE brushes. In contrast, snapshots of 10-down runs (Fig. 4(b)) show that the 10-domain was often more prominently oriented towards the surface, which then positions the 9-domain above the brush into the solution.

To highlight the interacting residues, trajectories of each residue's centre-of-mass height positions were plotted as heat maps. For the 9-down configuration (see exemplars in Fig. 5(a)), several residue segments within the 9-domain (residues 1–89) were consistently found at lower height positions from between 35 ns to 130 ns till the end of the 200 ns simulations, which resulted in prominent bands extending across the end of the plots (*i.e.*, towards longer simulation times). Several lighter bands were also observed between residues 90–184 of the 10–domain, indicating also consistent interactions but reduced penetration into the peptoid layer. The locations of these residue band positions appear to be common for both PSKE and PS surfaces and at both low and high chain densities. Moreover, for 10-down configurations (Fig. 5(b)), the same residue segments in $FnIII_{10}$ became the prominent bands while no bands in the 9-domain were seen close to the surface, corroborating the orientation of the domains seen in MD snapshots.

To narrow down the protein residue segments most closely interacting with PSKE and PS, the centre-of-mass height differences between the full protein and each individual protein residue were calculated and averaged for the final 50 ns of the

Table 2 Number of simulations with $FnIII_9$ down, $FnIII_{10}$ down, or even

Surface	9-down	10-down	Even
PS, Nchain = 12	2	4	3
PS, Nchain = 60	2	4	3
PS (all)	4	8	6
PSKE, Nchain = 12	2	3	4
PSKE, Nchain = 60	3	3	3
PSKE (all)	5	6	7

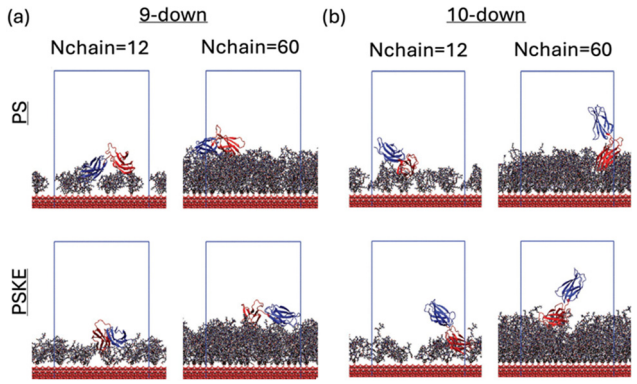

Fig. 4 Exemplar snapshots with (a) 10-down interactions (for PS: Nchain = 12 – run 5, Nchain = 60 – run 1; for PSKE: Nchain = 12 – run 9, Nchain = 60 – run 3), and (b) 9-down interactions (for PS: Nchain = 12 – run 6, Nchain = 60 – run 4; for PSKE: Nchain = 12 – run 7, Nchain = 60 – run 7).

trajectories (see Fig. 5(c) and (d) for exemplar trends; all data shown in Fig. S5a–d). In the 9-down configuration, I23–I29 and N76–G86 in $FnIII_9$ were oriented closest to the peptoids and farthest away from the protein centre of mass (Fig. 5(c)). Table 3 lists the sequences, which are referred as segments 9a and 9b in later discussions. The residues at the C-terminus linker region were also very close to the peptoid but these may not be relevant for the full multimeric fibronectin. In the 10-down configuration, A102–L109 and T148–G151 in $FnIII_{10}$, named segments 10a and 10b, respectively, were the most prominent and closest to the peptoids (Fig. 5(d) and Table 3).

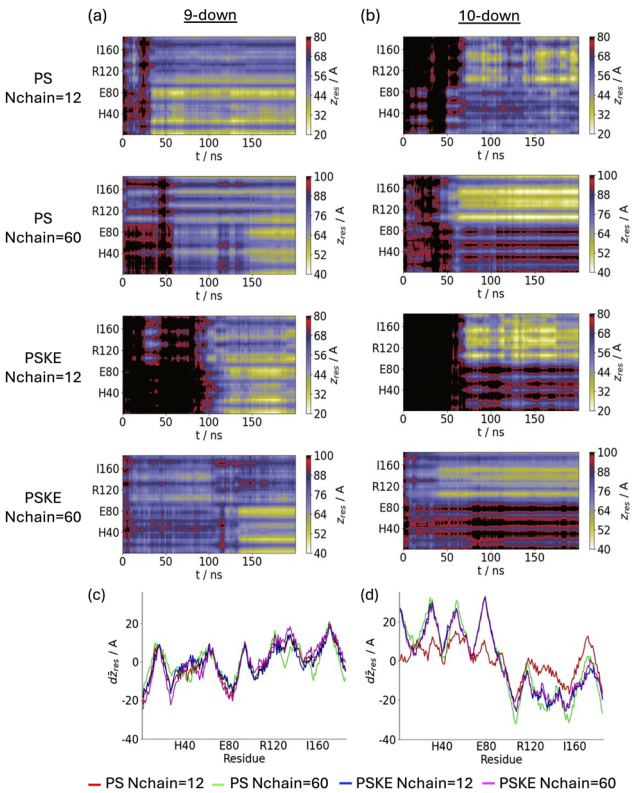

Fig. 5 (a) and (b) Trajectories of the height positions of individual residues (z_{res}, *i.e.*, surface-proximity) from exemplar simulation runs of, respectively, 9-down and 10-down configurations. From top of bottom, the rows correspond to PS Nchain = 12, PS Nchain = 60, PSKE Nchain = 12, and PSKE Nchain = 60. The specific runs for each combination of peptoid, chain and 9- or 10-down configuration correspond to those shown in Fig. 4. (c) and (d) Difference in height positions between the centres-of-mass of individual residues and $FnIII_{9\text{-}10}$ (Δz_{res}, *i.e.*, relative proximity), averaged over the final 50 ns, for, respectively, the 9-down and 10-down exemplar runs shown in (a) and (b).

Given the almost even protein orientation in the 9-down configuration, segments 10a and 10b were also found closer to the peptoid (Fig. 5(c)). Indeed, in the 9-down configuration all minima and maxima in residue height difference resided between ±20 Å. In contrast, in the 10-down configuration, while all 10-domain residues were all roughly at or below 0 Å (the centre-of-mass position), the 9-domain residues were all positioned at or above 0 Å.

An additional snapshot highlighting the peptoid interaction segments is shown in Fig. S5e, and it is seen that they are located towards the ends of the 9- and 10-domains, corroborating the protein orientations seen MD snapshots (Fig. 4). Notably, Fig. S5e also highlights that the functionally important synergy (PHRSN) and cell binding (RGD) motifs faced away from the surface, and examination of other trajectories show this to be the case in general.

Since the aforementioned interaction segments contain a number of polar and charged residues, electrostatic and dipole interactions may be the main contributions to the attractive interactions (see further discussion in section 3.3). Moreover, some of the interacting segments overlap with past studies. For example, simulations of $FnIII_{8\text{–}10}$ found that T104–T106 of the 10-domain was associated with adsorption onto a polar (OH-terminated) self-assembled monolayers (SAM).[64] In another study, T106 and G151 (as well as N132 and G136) were found to be involved in $FnIII_{9\text{-}10}$ adsorption onto an OH-terminated SAM.[65]

Fig. 5(c) and (d) also indicate potential differences between the overall protein interactions between the zwitterionic PSKE and uncharged PS. For example, there were obvious differences in the trends for PS between the Nchain = 12 and Nchain = 60 chain densities, especially in the 10-down configuration (Fig. 5(d)). In contrast, the trends for PSKE were almost identical in both 9-down and 10-down simulations (Fig. 5(c) and (d)). Moreover, the fact that all runs with different starting protein orientations identified the same interaction segments gives confidence that the simulations were long enough for the system to sample the most favourable interacting residues, and

Table 3 Key protein regions and residues for protein interaction with peptoid brushes identified in residue-surface proximity analysis (Fig. 5 and Fig. S5)

Domain	Region	Residues
$FnIII_9$	I23–I29 (segment 9a)	IAPRATI
	N76–G86 (segment 9b)	NGREESPLLIG
$FnIII_{10}$	A102–L109 (segment 10a)	AATPTSLL
	T148–G151 (segment 10b)	TISG

there may indeed be a degree of specificity for interactions with PSKE.

3.3. Specificity in hydrogen bonding interactions

To examine the specificity of hydrogen bond interaction, Fig. 6 shows the frequency of hydrogen bond formation, *i.e.* number of times with which each type of amino acid residue in $FnIII_{9\text{-}10}$ was found to form hydrogen bonds (H-bonds) with PSKE and PS at the different chain densities. The specific residues are given in Table S3, which further lists whether the residues correspond to the previously identified interaction segments. The frequency for each *peptoid* residue was found to form H-bonds with the protein is shown in Fig. 7. The number of H-bonds counted for each run and the averages for each combination of peptoid and chain density are also given in Fig. S6.

Across the figures, it is clearly seen that the protein makes many fewer H-bonds with PS (Fig. 6(a), (b) and 7(a), (b)) than with PSKE (Fig. 6(c), (d) and 7(c), (d)). Also, as expected, more H-bonds were found at the higher chain densities for both PSKE and PS (Fig. 6(b), (d) and 7(b), (d)). In addition, Fig. 6 indicates specific patterns of protein residue H-bonding for the two peptoids.

In terms of the overall number of H-bonds, the averages for PS at Nchain = 12 and Nchain = 60 were 2.9 and 3.3 bonds, respectively; for PSKE at Nchain = 12 and Nchain = 60, there were 6.3 and 12.2 bonds, respectively (Fig. S6). This data correlated with the observation of the more negative energies for the Nchain = 60 surfaces (Fig. 3 and Fig. S3). The increased number of H-bonds for PSKE also correlated with the generally (slightly) more negative interaction energies found for this zwitterionic sequence. The chain density effect was expected since there were simply more chains for interaction at the higher brush density. The sequence specificity could be expected to arise from the Nk and Ne residues in PSKE, which are analogues of lysine (K) and glutamic acid (E), respectively, and can engage as both H-bond donors and acceptors with the protein residues. In contrast, the Na residues forming the backbones of both PS and PSKE, analogue of alanine (A), can only engage the protein as H-bond acceptors through the amide oxygen and nitrogen atoms along the peptoid backbone.

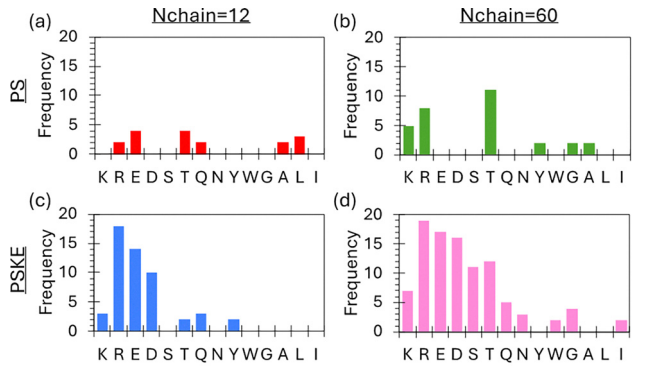

Fig. 6 The number of simulations ("frequency") in which H-bond interactions with the peptoid were found for each type of amino acid where interactions were observed: (a) PS, Nchain = 12, (b) PS, Nchain = 60, (c) PSKE, Nchain = 12, and (d) PSKE, Nchain = 60. The frequency was summed across the simulations performed for each peptoid and chain density combination.

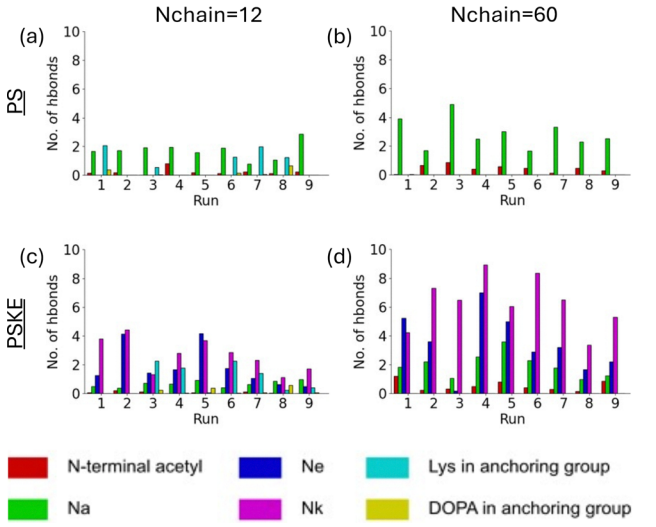

Fig. 7 Average number of H-bonds formed for different types of peptoid residues for each simulation run: (a) PS, Nchain = 12, (b) PS, Nchain = 60, (c) PSKE, Nchain = 12, and (d) PSKE, Nchain = 60.

The larger interaction energies observed for PSKE at Nchain = 60 and the significantly higher frequency of H-bonds found in those simulations might also be related to an the unexpected increase in experimentally measured protein adsorption observed on PSKE (and PMKE) as chain density increased to around 0.8 chain nm^{-2}, but not on PS (Fig. S1c). At these densities, the chains are only separated $\sim$1.2 nm apart, near the close packed distance of the surface anchoring group. Hence, the reduced chain mobility at very high grafting densities may increase binding with proteins if specific interactions were present, as indicated by MD simulations (different proteins may exhibit their own specific interaction sequences).

For the present $FnIII_{9\text{-}10}$, three amino acids—threonine (T), arginine (R), and alanine (A)—were found to form H-bonds with the elementary PS peptoid across both chain densities (Fig. 6(a) and (b)). These residues are characterized by sidechains terminating in, respectively, a branched unit with hydroxyl and methyl groups, a guanidinium group, and a methylene group. H-bonds for T were especially prominent. Some H-bonds for lysine (K) and glutamic acid (E) were also observed variously at the two chain densities. For PSKE, commonalities in T and R were also observed across the chain densities, but unlike with the uncharged PS, H-bonds with R were as prominent as those for T. Additional commonalities were observed at both PSKE chain densities for K, E, aspartic acid (D), and glutamine (Q), with those for E and D being especially prominent.

These observations match well with the protein interaction segments identified in the residue surface proximity analysis (Table 3). The T residues with H-bonds with PSKE at both densities correspond to segments 10a and 10b in the 10-domain and the segment 9a in the 9-domain. With PS, the

threonines correspond to segment 10b at both chain densities and to segment 10a at Nchain = 60. Some interacting T residues in the linker region and at various positions along the protein sequence were also found in a few of the runs. The R residues with H-bonds interacting with PSKE were found in both segments 9a and 9b, or in one of these segments for interactions with PS depending on the chain density. A few H-bonded arginines were further found close to the linker region (adjacent to the C-terminus) and at various positions depending the peptoid type and chain density. The other cationic residue K was most commonly found immediately preceding segment 10b. The anionic E and D residues were most commonly found in segment 10a but also in segment 9b. Q residues with H-bonds with PSKE were found in segment 9b.

We have previously found a tendency for the bulkier Nk and Ne peptoid residues to be concentrated at the brush's top surface to reduce steric hindrance and the electrostatic potential of the system,[36] which can further predispose PSKE to engage with oppositely charged protein residues. Specificities for peptoids and additionally for PSKE were also suggested by the facts that H-bonds with serine (S) and asparagine (N), both being able to engage as H-bond donors and acceptors and variants of, respectively T and Q, were not observed at all for PS and were only observed for PSKE at the higher Nchain = 60 density.

Specificity for the higher chain density may furthermore be related to the peptoid sequence. It can be seen in Fig. 6(d) that more of the interactions arise from Nk for Nchain = 60. This could be due to Nk being one residue closer to the N-terminus (Fig. 1(a)) and it would be more frequently exposed at the top of the brush. Correspondingly, the combined frequency of H-bonded glutamic acid (E) and aspartic acid (D) residues on the protein, oppositely charged to Nk, was also seen to be higher (Fig. 6(c) and (d)) than the combined frequency of lysines (K) and arginine (R) for engaging with Ne.

In addition to direct H-bonding, some water molecules can simultaneously H-bond with a protein and a peptoid residue, contributing a component to interfacial water that can also strongly determine protein–surface interactions. Just as for direct H-bonds, the numbers of these bridging water molecules are observed to be more numerous for the zwitterionic PSKE than the uncharged PS, and more numerous when there is a higher density of chains (Fig. S7). While the numbers of bridging and direct H-bonds are similar for PSKE, more bridging H-bonds are observed for PS. Nonetheless, at corresponding chain densities, more direct H-bonds are still counted for PSKE than there are bridging bonds counted for PS, and no correlation is apparent between the numbers of direct and bridging H-bonds in the simulation runs.

Overall, the simulations suggest that direct peptoid H-bonding with T (and less prominently, R) may be a common feature of peptoid interactions with $FnIII_{9\text{-}10}$, and possibly other proteins as well, since these are common canonical residues. Furthermore, due to the inclusion of Nk and Ne in the PSKE sequence, additional interactions with the charged amino acids K, E, D and also R were observed to be characteristic of this peptoid. These additional specific H-bonds might have also further contributed to the increased amount of proteins observed on the zwitterionic peptoid at near close-packed chain densities (Fig. 1(c) and Fig. S1). While bridging H-bonds increase the general number of interactions, they appear to be uncorrelated with the direct H-bonding interactions.

3.4. Fibronectin mobility on peptoid brushes

A central feature of fibronectin is its multimerization/assembly into fibrils, for which diffusion on the surface is required. Comparison between the in-plane motion of $FnIII_{9\text{-}10}$ on the different surfaces (Fig. 8) suggests that the protein is more mobile among the Nchain = 12 chains, consistent with the energetics and H-bonding analysis in earlier sections. The in-plane diffusion coefficient (D_{xy}) were also calculated from the trajectories (Fig. S8), and the highest mobilities corresponded to the sparser Nchain = 12 layers. Additionally, a narrower variation in D_{xy} was seen for the zwitterionic PSKE, corroborating the smaller in-plane motions shown visually in Fig. 8. Thus, while strong specific interactions with $FnIII_{9\text{-}10}$ were found for PSKE, the chain density might need to be optimised in experiments to confer appropriate protein surface mobility for controlling fibronectin fibril formation.

We further examined whether the lifetimes of direct H-bonds formed between the protein and peptoid chains may be linked to protein mobility (see Fig. S9 for H-bond time autocorrelation ($c(t)$) functions). We find that the decay of $c(t)$ is significantly slower (*i.e.*, generally higher lifetimes) than that seen for water–peptoid H-bonds,[36] indicative of specific brush interactions. Secondly, H-bond lifetimes for the higher density brushes are typically higher than for the lower density cases, consistent with the higher interaction energies, and lower mobilities and D_{xy} values seen. However, at corresponding chain densities, the range of lifetimes on PSKE tend to be shorter than on PS, suggesting that PSKE could be more effective as an antifouling brush but also that it might allow more protein movement at short lengthscales.

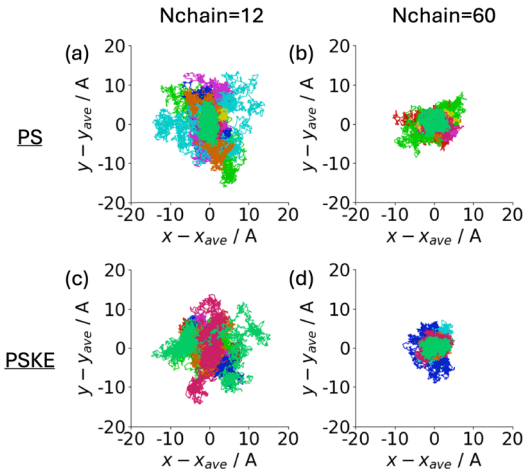

Fig. 8 Protein motion in *xy*-plane over last 50 ns of each simulation for PS, Nchain = 12 (a), PS, Nchain = 60 (b), PSKE, Nchain = 12 (c), and PSKE, Nchain = 60 (d). Black, red, green, blue, yellow, purple, turquoise, cyan, and magenta denote runs 1–9 respectively.

4. Conclusions

This is the first atomistic MD simulation of peptoid interactions with a protein. The system was based on the fibronectin $FnIII_{9\text{-}10}$ tandem domain interacting with a zwitterionic PSKE peptoid brush and its uncharged hydrophilic control PS (*i.e.*, polysarcosine, a potential alternative to PEG). The chain densities simulated were informed by experimental measurements of protein adsorption. Overall correspondence of the simulations with expected brush behaviour was confirmed by, *e.g.*, protein penetration at low peptoid chain density and increases in calculated interaction energy with penetration distance.

Interestingly, larger interaction energies were observed with the zwitterionic PSKE, which were consistently guided by four protein residue segments, two each in the 9- and 10-domains. This led to a consistent final ''flat'' protein configuration on the PSKE brush regardless of the starting protein orientation. The relative differences in interaction energies also correlated with the numbers of both direct and bridging H-bonds found between the protein and the peptoid, with more H-bonds found for PSKE than for PS and when more chains were present. Bridging H-bonds reflect a component of interfacial water that can play a key role in the binding of proteins to surfaces. While the present MM-PBSA calculations of interaction energies neglect the interfacial water contribution and other effects, the overall simulation results should be reflective of $FnIII_{9\text{-}10}$ interactions with the peptoid surfaces.

In particular, H-bonds with PSKE were more frequently found for specific amino acids—threonine (T) but not serine (S), arginine (R) but not lysine (K), and glutamic (E) and aspartic acids (D)—in the high interaction segments of both 9- and 10-domains. In contrast, PS tended to interact with the protein in a ''10-down'' configuration. Nonetheless, specificity for the interaction segments remained, focused on T and R. Since these are common canonical amino acids and PS represents the elementary peptoid backbone, T and R H-bonds could be characteristic of peptoid–protein interactions. Additional specificity could then be conferred by PSKE with its charged residues and a penultimate cationic Nk peptoid residue sequenced near the top of the PSKE brush to promote interactions with E and D residues on $FnIII_{9\text{-}10}$.

Overall, our MD analysis has revealed that specific fibronectin residues can drive specific interactions with the peptoids PSKE and PS beyond general considerations of hydrophobicity and charge. The larger interaction energies and the higher number of H-bonds seen with PSKE could promote protein binding, as reflected in an increased amount of surface bound proteins now measured on PSKE but not PS at very high chain densities. While different interaction sequence segments would be expected for different proteins, the present simulations show that the $FnIII_{9\text{-}10}$ interaction segments should be able to orient the biologically relevant synergy (PHRSN) and cell binding (RGD) motifs ''up'' for interactions with cells. They further show that the chain density can be used to modify protein mobility, which can be important for promoting fibronectin multimerization into extracellular matrix fibrils. Therefore, the zwitterionic PSKE can be evaluated in future cell culture experiments for mediating cell adhesion.

Author contributions

Conceptualization: DC, KHAL; methodology-experimental: PBM, KHAL; methodology-computation: DC; investigation: DC; writing: DC, KHAL.

Conflicts of interest

There are no conflicts to declare.

Data availability

All data presented in this work, including simulation files and analysis scripts, are available from the University of Strathclyde Knowledge Base at **https://doi.org/10.15129/11105fc7-894c-4298-85a7-abf7ed4bfd89**.

Supplementary information including experimental protocols and additional simulation analyses, are available. See DOI: **https://doi.org/10.1039/d5cp02324f**.

Acknowledgements

Computational resources were provided by the SFI/HEA funded Irish Centre for High End Computing. DC and KHAL thank the Royal Society of Edinburgh for Saltire International Collaboration research support (ref. 1979). PBM acknowledges support by grant number R01 EB005772 from the National Institute of Biomedical Imaging and Bioengineering (NIBIB) at the National Institutes of Health (NIH). KHAL acknowledges support by fellowship number HL104966 from the National Heart, Blood and Lung Institute (NHBLI) at the NIH.

References

1 A. M. C. Maan, A. H. Hofman, W. M. De Vos and M. Kamperman, Recent Developments and Practical Feasibility of Polymer-Based Antifouling Coatings, *Adv. Funct. Mater.*, 2020, **30**, 2000936.
2 X. Xu, Y. Chang, Y. Gong, Y. Zhang, Y. Yu, H. Peng and C. Fu, Recent Advances in Antifouling Surface Polymer Brushes, *ACS Appl. Polym. Mater.*, 2024, **6**, 1–27.
3 J. Lisoń, A. Taratuta, Z. Paszenda, M. Szindler and M. Basiaga, Perspectives in Prevention of Biofilm for Medical Applications, *Coatings*, 2022, **12**, 197.
4 W. L. Murphy, T. C. McDevitt and A. J. Engler, Materials as stem cell regulators, *Nat. Mater.*, 2014, **13**, 547–557.
5 A. Rodrigo-Navarro, S. Sankaran, M. J. Dalby, A. Del Campo and M. Salmeron-Sanchez, Engineered living biomaterials, *Nat. Rev. Mater.*, 2021, **6**, 1175–1190.
6 C. Blaszykowski, S. Sheikh and M. Thompson, Surface chemistry to minimize fouling from blood-based fluids, *Chem. Soc. Rev.*, 2012, **41**, 5599.

7 C. Rodriguez-Emmenegger, E. Brynda, T. Riedel, M. Houska, V. Šubr, A. B. Alles, E. Hasan, J. E. Gautrot and W. T. S. Huck, Polymer Brushes Showing Non-Fouling in Blood Plasma Challenge the Currently Accepted Design of Protein Resistant Surfaces, *Macromol. Rapid Commun.*, 2011, **32**, 952–957.
8 J. Ci, H. Kang, C. Liu, A. He and R. Liu, Protein resistance adsorption mechanism and applications of zwitterionic polymers, *Prog. Chem.*, 2015, **27**, 1198–1212.
9 S. Chen, L. Li, C. Zhao and J. Zheng, Surface hydration: Principles and applications toward low-fouling/nonfouling biomaterials, *Polymer*, 2010, **51**, 5283–5293.
10 R. J. Simon, R. S. Kania, R. N. Zuckermann, V. D. Huebner, D. A. Jewell, S. Banville, S. Ng, L. Wang, S. Rosenberg and C. K. Marlowe, Peptoids: a modular approach to drug discovery, *Proc. Natl. Acad. Sci. U. S. A.*, 1992, **89**, 9367–9371.
11 R. N. Zuckermann, Peptoid origins, *Biopolymers*, 2011, **96**, 545–555.
12 K. H. A. Lau, C. Ren, T. S. Sileika, S. H. Park, I. Szleifer and P. B. Messersmith, Surface-grafted polysarcosine as a peptoid antifouling polymer brush, *Langmuir*, 2012, **28**, 16099–16107.
13 J. Wang, Y. Ding, K. Chong, M. Cui, Z. Cao, C. Tang, Z. Tian, Y. Hu, Y. Zhao and S. Jiang, Recent Advances in Lipid Nanoparticles and Their Safety Concerns for mRNA Delivery, *Vaccines*, 2024, **12**, 1148.
14 Y. Hu, Y. Hou, H. Wang and H. Lu, Polysarcosine as an Alternative to PEG for Therapeutic Protein Conjugation, *Bioconjugate Chem.*, 2018, **29**, 2232–2238.
15 K. H. A. Lau, T. S. Sileika, S. H. Park, A. M. L. Sousa, P. Burch, I. Szleifer and P. B. Messersmith, Molecular Design of Antifouling Polymer Brushes Using Sequence-Specific Peptoids, *Adv. Mater. Interfaces*, 2015, **2**, 1400225.
16 J. Sun and R. N. Zuckermann, Peptoid Polymers: A Highly Designable Bioinspired Material, *ACS Nano*, 2013, **7**, 4715–4732.
17 M. F. Mora, J. L. Wehmeyer, R. Synowicki and C. D. Garcia, in *Biological Interactions on Materials Surfaces*, ed. D. A. Puleo and R. Bizios, Springer, US, New York, NY, 2009, pp. 19–41.
18 D. Shen, M. Huang, L.-M. Chow and M. Yang, Kinetic profile of the adsorption and conformational change of lysozyme on self-assembled monolayers as revealed by quartz crystal resonator, *Sens. Actuators, B*, 2001, **77**(3), 664–670.
19 P. Böhm, A. Koutsioubas, J.-F. Moulin, J. O. Rädler, E. Sackmann and B. Nickel, Probing the Interface Structure of Adhering Cells by Contrast Variation Neutron Reflectometry, *Langmuir*, 2019, **35**, 513–521.
20 F. Pan, K. H. Aaron Lau, P. B. Messersmith, J. R. Lu and X. Zhao, Interfacial Assembly Inspired by Marine Mussels and Antifouling Effects of Polypeptoids: A Neutron Reflection Study, *Langmuir*, 2020, **36**, 12309–12318.
21 T. Weidner and D. G. Castner, SFG analysis of surface bound proteins: a route towards structure determination, *Phys. Chem. Chem. Phys.*, 2013, **15**, 12516–12524.
22 H. Geng, P. Zhang, Q. Peng, J. Cui, J. Hao and H. Zeng, Principles of Cation–π Interactions for Engineering Mussel-Inspired Functional Materials, *Acc. Chem. Res.*, 2022, **55**, 1171–1182.
23 D. Alsteens, Probing living cell dynamics and molecular interactions using atomic force microscopy, *Biophys. Rev.*, 2024, **16**, 663–677.
24 L. Wang, Y. Qian, Y. Sun, B. Liu and G. Wei, Single-molecule force spectroscopy: A facile technique for studying the interactions between biomolecules and materials interfaces, *Rev. Anal. Chem.*, 2020, **39**, 116–129.
25 M. Ozboyaci, D. B. Kokh, S. Corni and R. C. Wade, Modeling and simulation of protein-surface interactions: Achievements and challenges, *Q. Rev. Biophys.*, 2016, **49**, 1–45.
26 M. Penna, K. Ley, S. Maclaughlin and I. Yarovsky, Surface heterogeneity: a friend or foe of protein adsorption – insights from theoretical simulations, *Faraday Discuss.*, 2016, **191**, 435–464.
27 D. L. Cheung, Effect of surface structure on peptide adsorption on soft surfaces, *Chem. Phys. Lett.*, 2020, **758**, 137929.
28 K. Kubiak-Ossowska, P. A. Mulheran and W. Nowak, Fibronectin Module FNIII9 Adsorption at Contrasting Solid Model Surfaces Studied by Atomistic Molecular Dynamics, *J. Phys. Chem. B*, 2014, **118**, 9900–9908.
29 G. Brancolini, A. Corazza, M. Vuano, F. Fogolari, M. C. Mimmi, V. Bellotti, M. Stoppini, S. Corni and G. Esposito, Probing the Influence of Citrate-Capped Gold Nanoparticles on an Amyloidogenic Protein, *ACS Nano*, 2015, **9**, 2600–2613.
30 K. Kubiak-Ossowska, K. Tokarczyk, B. Jachimska and P. A. Mulheran, Bovine Serum Albumin Adsorption at a Silica Surface Explored by Simulation and Experiment, *J. Phys. Chem. B*, 2017, **121**, 3975–3986.
31 M. K. Bieniek, V. Llopis-Hernandez, K. Douglas, M. Salmeron-Sanchez and C. D. Lorenz, Minor Chemistry Changes Alter Surface Hydration to Control Fibronectin Adsorption and Assembly into Nanofibrils, *Adv. Theory Simul.*, 2019, **2**, 1900169.
32 C. P. O. ' Brien, S. J. Stuart, D. A. Bruce and R. A. Latour, Modeling of Peptide Adsorption Interactions with a Poly (lactic acid) Surface Modeling of Peptide Adsorption Interactions with a Poly (lactic acid), *Langmuir*, 2008, **24**, 14115–14124.
33 D. Mallinson, D. L. Cheung, D. Simionesie, A. B. Mullen, Z. J. Zhang and D. A. Lamprou, Experimental and computational examination of anastellin (FnIII1c)-polymer interactions, *J. Biomed. Mater. Res., Part A*, 2017, **105**, 737–745.
34 X. Song, J. Man, Y. Qiu, J. Wang, R. Li, Y. Zhang, G. Cui, J. Li, J. Li and Y. Chen, Study of Hydration Repulsion of Zwitterionic Polymer Brushes Resistant to Protein Adhesion through Molecular Simulations, *ACS Appl. Mater. Interfaces*, 2024, **16**, 17145–17162.
35 S. Sheikh, C. Blaszykowski, R. Nolan, D. Thompson and M. Thompson, On the hydration of subnanometric antifouling organosilane adlayers: A molecular dynamics simulation, *J. Colloid Interface Sci.*, 2015, **437**, 197–204.
36 D. L. Cheung and K. H. A. Lau, Atomistic Study of Zwitterionic Peptoid Antifouling Brushes, *Langmuir*, 2019, **35**, 1483–1494.

37 C. J. Dalton and C. A. Lemmon, Fibronectin: Molecular Structure, Fibrillar Structure and Mechanochemical Signaling, *Cells*, 2021, **10**, 2443.
38 A. Josyula, K. S. Parikh, I. Pitha and L. M. Ensign, Engineering biomaterials to prevent post-operative infection and fibrosis, *Drug Deliv. Transl. Res.*, 2021, **11**, 1675–1688.
39 M. Salmerón-Sánchez, P. Rico, D. Moratal, T. T. Lee, J. E. Schwarzbauer and A. J. García, Role of material-driven fibronectin fibrillogenesis in cell differentiation, *Biomaterials*, 2011, **32**, 2099–2105.
40 V. Llopis-Hernández, M. Cantini, C. González-García, Z. A. Cheng, J. Yang, P. M. Tsimbouri, A. J. García, M. J. Dalby and M. Salmerón-Sánchez, Material-driven fibronectin assembly for high-efficiency presentation of growth factors, *Sci. Adv.*, 2016, **2**, e1600188.
41 D. J. Vaca, A. Thibau, M. Schütz, P. Kraiczy, L. Happonen, J. Malmström and V. A. J. Kempf, Interaction with the host: the role of fibronectin and extracellular matrix proteins in the adhesion of Gram-negative bacteria, *Med. Microbiol. Immunol.*, 2020, **209**, 277–299.
42 H. W. A. Swanson, K. H. A. Lau and T. Tuttle, Minimal Peptoid Dynamics Inform Self-Assembly Propensity, *J. Phys. Chem. B*, 2023, **127**, 10601–10614.
43 H. W. A. Swanson, K. H. A. Lau and T. Tuttle, *A Convention for Peptoid Monomer Naming*, University of Strathclyde, 2023.
44 D. J. Leahy, I. Aukhil and H. P. Erickson, 2.0 Å Crystal Structure of a Four-Domain Segment of Human Fibronectin Encompassing the RGD Loop and Synergy Region, *Cell*, 1996, **84**, 155–164.
45 A. D. MacKerell, D. Bashford, R. L. Dunbrack, J. D. Evanseck, M. J. Field, S. Fischer, J. Gao, H. Guo, S. Ha, D. Joseph-McCarthy, L. Kuchnir, K. Kuczera, F. T. K. Lau, C. Mattos, S. Michnick, T. Ngo, D. T. Nguyen, B. Prodhom, W. E. Reiher, B. Roux, M. Schlenkrich, J. C. Smith, R. Stote, J. Straub, M. Watanabe, J. Wiórkiewicz-Kuczera, D. Yin, M. Karplus, R. L. Dunbrack, J. D. Evanseck, M. J. Field, S. Fischer, J. Gao, H. Guo, S. Ha, D. Joseph-McCarthy, L. Kuchnir, K. Kuczera, F. T. K. Lau, C. Mattos, S. Michnick, T. Ngo, D. T. Nguyen, B. Prodhom, W. E. Reiher, B. Roux, M. Schlenkrich, J. C. Smith, R. Stote, J. Straub, M. Watanabe, J. Wiórkiewicz-Kuczera, D. Yin and M. Karplus, All-Atom Empirical Potential for Molecular Modeling and Dynamics Studies of Proteins, *J. Phys. Chem. B*, 1998, **102**, 3586–3616.
46 D. T. Mirijanian, R. V. Mannige, R. N. Zuckermann and S. Whitelam, Development and use of an atomistic CHARMM-based forcefield for peptoid simulation, *J. Comput. Chem.*, 2014, **35**, 360–370.
47 D. Gfeller, O. Michielin and V. Zoete, SwissSidechain: A molecular and structural database of non-natural sidechains, *Nucleic Acids Res.*, 2013, **41**, 327–332.
48 P. Mark and L. Nilsson, Structure and dynamics of the TIP3P, SPC, and SPC/E water models at 298 K, *J. Phys. Chem. A*, 2001, **105**, 9954–9960.
49 M. Predota, A. V. Bandura, P. T. Cummings, J. D. Kubicki, D. J. Wesolowski, A. A. Chialvo and M. L. Machesky, Electric Double Layer at the Rutile (110) Surface. 1. Structure of Surfaces and Interfacial Water from Molecular Dynamics by Use of ab Initio Potentials, *J. Phys. Chem. B*, 2004, **108**, 12049–12060.
50 U. Essmann, L. Perera, M. L. Berkowitz, T. Darden, H. Lee and L. G. Pedersen, A smooth particle mesh Ewald method, *J. Chem. Phys.*, 1995, **103**, 8577.
51 D. Van Der Spoel, E. Lindahl, B. Hess, G. Groenhof, A. E. Mark and H. J. C. Berendsen, GROMACS: Fast, flexible, and free, *J. Comput. Chem.*, 2005, **26**, 1701–1718.
52 B. Hess, C. Kutzner, D. van der Spoel and E. Lindahl, GROMACS 4: Algorithms for Highly Efficient, Load-Balanced, and Scalable Molecular Simulation, *J. Chem. Theory Comput.*, 2008, **4**, 435–447.
53 M. J. Abraham, T. Murtola, R. Schulz, S. Páll, J. C. Smith, B. Hess and E. Lindahl, GROMACS: High performance molecular simulations through multi-level parallelism from laptops to supercomputers, *SoftwareX*, 2015, **1–2**, 19–25.
54 G. Bussi, D. Donadio and M. Parrinello, Canonical sampling through velocity rescaling, *J. Chem. Phys.*, 2007, **126**, 014101.
55 B. Hess, H. Bekker, H. J. C. Berendsen and J. G. E. M. Fraaije, LINCS: A linear constraint solver for molecular simulations, *J. Comput. Chem.*, 1997, **18**, 1463–1472.
56 S. Miyamoto and P. A. Kollman, Settle: An analytical version of the SHAKE and RATTLE algorithm for rigid water models, *J. Comput. Chem.*, 1992, **13**, 952–962.
57 N. Michaud-Agrawal, E. J. Denning, T. B. Woolf and O. Beckstein, MDAnalysis: A Toolkit for the Analysis of MolecularDynamics Simulations, *J. Comput. Chem.*, 2011, **32**, 2319–2327.
58 W. Humphrey, A. Dalke and K. Schulten, VMD: Visual molecular dynamics, *J. Mol. Graphics*, 1996, **14**, 33–38.
59 J. Srinivasan, T. E. Cheatham, P. Cieplak, P. A. Kollman and D. A. Case, Continuum Solvent Studies of the Stability of DNA, RNA, and Phosphoramidate–DNA Helices, *J. Am. Chem. Soc.*, 1998, **120**, 9401–9409.
60 T. Hou, J. Wang, Y. Li and W. Wang, Assessing the Performance of the MM/PBSA and MM/GBSA Methods. 1. The Accuracy of Binding Free Energy Calculations Based on Molecular Dynamics Simulations, *J. Chem. Inf. Model.*, 2011, **51**, 69–82.
61 D. Sitkoff, K. A. Sharp and B. Honig, Accurate Calculation of Hydration Free Energies Using Macroscopic Solvent Models, *J. Phys. Chem.*, 1994, **98**, 1978–1988.
62 B. R. Miller, T. D. McGee, J. M. Swails, N. Homeyer, H. Gohlke and A. E. Roitberg, *MMPBSA.py*: An Efficient Program for End-State Free Energy Calculations, *J. Chem. Theory Comput.*, 2012, **8**, 3314–3321.
63 J. Kyte and R. F. Doolittle, A simple method for displaying the hydropathic character of a protein, *J. Mol. Biol.*, 1982, **157**, 105–132.
64 E. Liamas, K. Kubiak-Ossowska, R. Black, O. Thomas, Z. Zhang and P. Mulheran, Adsorption of Fibronectin Fragment on Surfaces Using Fully Atomistic Molecular Dynamics Simulations, *Int. J. Mol. Sci.*, 2018, **19**, 3321.
65 T. Li, L. Hao, J. Li, C. Du and Y. Wang, Role of Ninth Type-III Domain of Fibronectin in the Mediation of Cell-Binding Domain Adsorption on Surfaces with Different Chemistries, *Langmuir*, 2018, **34**, 9847–9855.